



## An active-fire based burned area mapping algorithm for the MODIS sensor

Louis Giglio <sup>a,b,\*</sup>, Tatiana Loboda <sup>b</sup>, David P. Roy <sup>c</sup>, Brad Quayle <sup>d</sup>, Christopher O. Justice <sup>b</sup>

<sup>a</sup> Science Systems and Applications, Inc., Lanham, Maryland, USA

<sup>b</sup> Department of Geography, University of Maryland, College Park, Maryland, USA

<sup>c</sup> Geographic Information Science Center of Excellence, South Dakota State University, Brookings, South Dakota, USA

<sup>d</sup> USDA Forest Service Remote Sensing Applications Center, Salt Lake City, Utah, USA

### ARTICLE INFO

#### Article history:

Received 23 June 2008

Received in revised form 9 October 2008

Accepted 11 October 2008

#### Keywords:

Fire

Biomass burning

Burn scar

Burned area

MODIS

### ABSTRACT

We present an automated method for mapping burned areas using 500-m Moderate Resolution Imaging Spectroradiometer (MODIS) imagery coupled with 1-km MODIS active fire observations. The algorithm applies dynamic thresholds to composite imagery generated from a burn-sensitive vegetation index and a measure of temporal texture. Cumulative active fire maps are used to guide the selection of burned and unburned training samples. An accuracy assessment for three geographically diverse regions (central Siberia, the western United States, and southern Africa) was performed using high resolution burned area maps derived from Landsat imagery. Mapped burned areas were accurate to within approximately 10% in all regions except the high-tree-cover sub-region of southern Africa, where the MODIS burn maps underestimated the area burned by 41%. We estimate the minimum detectable burn size for reliable detection by our algorithm to be on the order of 120 ha.

© 2008 Elsevier Inc. All rights reserved.

### 1. Introduction

The growing recognition of biomass burning as a widespread and significant agent of change in the Earth system has led to an ongoing need for long-term fire data at the regional, continental, and global scale. In part this demand has been met with a substantial body of satellite-based active fire observations made using a number of coarse- and medium-resolution sensors, initially the Advanced Very High Resolution Radiometer (AVHRR) (Dozier, 1981; Matson and Dozier, 1981), followed by the Geostationary Operational Environmental Satellite (GOES) Imager (Prins and Menzel, 1992), the Defense Meteorological Satellite Program (DMSP) Operational Linescan System (OLS) (Elvidge et al., 1996), the Along-Track Scanning Radiometer (ATSR) (Arino and Rosaz, 1999), the Visible and Infrared Scanner (VIIRS) (Giglio et al., 2000), the Moderate Resolution Imaging Spectroradiometer (MODIS) (Justice et al., 2002), and the Spinning Enhanced Visible and Infrared Imager (SEVIRI) (Roberts et al., 2005).

While active fire products capture information about the location and timing of fires burning at the time of the satellite overpass, they do not generally permit burned area to be reliably (or at least directly) estimated (Scholes et al., 1996; Eva and Lambin, 1998b; Kasischke et al., 2003; Giglio et al., 2006). Yet reliable, large-scale (usually global)

maps of burned area are essential for many applications, in particular the estimation of pyrogenic gaseous and aerosol emissions. This need has consequently prompted the development of numerous satellite-based methods for mapping burned areas, the majority of which operate without exploiting active fire information. Kasischke and French (1995), for example, applied differencing to 15-day AVHRR Normalized Difference Vegetation Index (NDVI) composite imagery to detect burns in Alaskan boreal forests during 1990 and 1991. Fernández et al. (1997) mapped large forest fires in Spain during 1993 and 1994 with 10-day AVHRR maximum-NDVI composites using separate regression and differencing techniques. Eva and Lambin (1998a) mapped burns in central Africa during the 1994–1995 dry season using 1-km ATSR imagery by matching decreases in short-wave infrared (SWIR) reflectance with increases in surface temperature. Barbosa et al. (1999) used daily 5-km AVHRR imagery to map burned areas in Africa based on changes occurring in reflectance, brightness temperature, and a vegetation index (VI). Pereira et al. (2000) used classification trees to map burned area in central Africa and Iberia with AVHRR thermal, albedo, and VI imagery; Stroppiana et al. (2003) applied a similar technique in Australian woodland savannas using 10-day SPOT VEGETATION (VGT) composites. Fraser et al. (2003) developed an approach for mapping burned boreal forest at the continental scale using 10-day VGT VI composites and a logistic regression model. The GLOBCAR global burned area product (Simon et al., 2004) was produced for the year 2000 using two different algorithms, one contextual and one fixed-threshold, applied to ATSR-2 and AATSR imagery. The GBA-2000 global burned area product was independently produced by Tansey et al. (2004) using a combination

\* Corresponding author. Science Systems and Applications, Inc., Lanham, Maryland, USA.

E-mail address: [louis\\_giglio@ssaihq.com](mailto:louis_giglio@ssaihq.com) (L. Giglio).

of nine different regional algorithms applied to 1-km VGT daily surface reflectance imagery. Roy et al. (2002, 2005b) developed a predictive bi-directional reflectance modeling approach to map burned areas on a daily basis using 500-m MODIS imagery. Most recently, Tansey et al. (2008) modified one of the regional GBA-2000 algorithms for global use to produce the L3JRC 1-km global burned area product for 2000–2007.

Although the majority of existing burned-area mapping methods do not exploit active fire information, a minority are *hybrid algorithms* which supplement the “standard” remotely-sensed indicators used for burn mapping (surface reflectance, surface temperature, NDVI, etc.) with active fire maps. Roy et al. (1999), for example, used AVHRR data to map savanna burns in southern Africa from a temporal composite of the range of a spectral index. Burned and unburned pixels were differentiated using a threshold based on the mean and standard deviation of the range of this index for pixels where active fires were detected. Similarly, in the Fraser et al. (2000) HANDS algorithm, which was designed for mapping boreal forest burns with AVHRR data, the expected change in successive 10-day NDVI composites for burned pixels was derived using an AVHRR active fire mask. A similar method was developed by Pu et al. (2004) for mapping burned areas in California, again with AVHRR data. George et al. (2006) used two different vegetation indexes derived from 16-day MODIS nadir BRDF-adjusted reflectance composites to detect burn scars in central Russia over a twelve year period. Disturbed landscape segments were identified using a contextual algorithm and NDVI differencing, and those segments containing active fires were classified as having burned. Lastly, Loboda et al. (2007) developed a method for mapping burned areas on an annual basis using 500-m MODIS 8-day surface reflectance composites and 1-km MODIS active fire masks. As with the Roy et al. (1999) approach, thresholds for burned pixels were derived from statistics computed for pixels where active fires were detected.

While the spatial and temporal information available from active fire data is intuitively useful for burned area mapping, active fire maps generally have several characteristics which complicate their use in hybrid algorithms, particularly those intended for use in multiple biomes. First, the minimum detectable size of an active fire is up to ~1000 times smaller than the minimum detectable size of a burned area (Giglio et al., 2006); selecting burned training pixels based on the occurrence of an active fire is therefore susceptible to contamination from pixels containing small, undetectable burned areas. Second, active-fire false alarms (i.e., commission errors) will also contaminate burned training samples. Third, whereas using active fire locations to guide the selection of burned training pixels is comparatively straightforward (e.g., Roy et al., 1999), considerably more care is required in selecting *unburned* training pixels, as the absence of detected fires at a particular location does not guarantee that the location did not burn. Active-fire omission errors can occur because fires are too small to detect, or are obscured by clouds or overstory vegetation, or were not actively burning at the time of the satellite overpass. This can lead to the inclusion of burned pixels in an unburned training sample selected on the basis of their (lack of) proximity to hot spots.

In this paper we present an automated hybrid algorithm for mapping burned areas using MODIS imagery which largely overcomes the above issues. The algorithm, which is a simplified version of an earlier prototype used by Giglio et al. (2006, Appendix A), detects persistent changes in a daily vegetation-index time series derived from MODIS surface reflectance observations. Maps of active fires are used to generate regional probability density functions suitable for classifying these persistent changes as either burned or unburned. The algorithm identifies the date of burn, to the nearest day, for pixels within individual MODIS Level 3 tiles (Section 2) at 500-m spatial resolution.

Although our algorithm is conceptually similar to the hybrid approaches mentioned above, it contains several innovations

intended to more fully exploit the information provided by active fire maps, enabling the algorithm to function more robustly over a wide range of biomes. Among these are the ability to identify training samples of both burned and unburned pixels, in part through a region growing phase, which also permits the algorithm to function in the presence of extremely large burned areas, and the use of both spectral and textural information to help discriminate between burned and unburned pixels. In addition, the algorithm operates within a Bayesian framework in which prior probabilities are adjusted based on the proximity of burned training pixels, further exploiting the information derived from active fire observations. To evaluate algorithm performance an accuracy assessment in three geographically diverse regions (Siberia, the United States, and southern Africa) using high resolution burned area maps manually derived from Landsat TM imagery was performed.

## 2. Data

The burned-area detection algorithm uses the Terra (“MOD09GHK”) and/or Aqua (“MYD09GHK”) 500-m MODIS atmospherically-corrected Level 2G daily surface reflectance products (Vermote and Justice, 2002), the 1-km Terra (“MOD14A1”) and/or Aqua (“MYD14A1”) MODIS Level 3 daily active fire products (Justice et al., 2002), and the Level 3 MODIS “MOD12Q1” 96-day land cover product (Friedl et al., 2002). The MODIS Level 2G and Level 3 products are defined on global 250 m, 500 m, and 1 km sinusoidal grids in fixed geolocated tiles approximately  $10^\circ \times 10^\circ$  in size (Wolfe et al., 1998).

## 3. Detection algorithm

The algorithm proceeds through several stages shown in Fig. 1, processing a single MODIS tile at a time. The general approach is to produce composite imagery summarizing persistent changes in the VI time series, and then use spatial and temporal active-fire information to guide the statistical characterization of burn-related and non-burn-related change within the scene. This information is used to estimate probabilistic thresholds suitable for classifying the scene into burned and unburned pixels.

The algorithm is nominally used to produce burned area maps for time periods of one to several months. Provided this period doesn't span more than a single fire season, the actual interval for which a map is produced may be selected solely on the basis of convenience. Regardless of the time period chosen, however, a minimum of approximately ten days of cloud-free observations before and after this period are required to accommodate the moving windows employed in the change-detection process. In practice, cloud obscuration and coverage gaps double the number of days of data needed before and after the mapping period to avoid potentially large omission errors in the resulting burned area maps.

### 3.1. Time series extraction

Valid daily band 1 ( $0.65\text{ }\mu\text{m}$ ), 5 ( $1.2\text{ }\mu\text{m}$ ), and 7 ( $2.1\text{ }\mu\text{m}$ ) reflectances are extracted from the Level 2G surface reflectance product. To be considered valid, each daily reflectance must meet the following criteria. First, the observation must be free from cloud contamination, as flagged in a separate quality-assessment layer of the Level 2G product. Second, the observation must not have been acquired on a day in which one or more active fires were detected in the 500-m grid cell being processed. This avoids potential contamination of the SWIR reflectances (particularly band 7) with an emissive fire component (Smith and Wooster, 2005). Third, the 500-m grid cell must be located on land. Finally, each reflectance must fall between 0 and 1, thus excluding both missing data (MODIS does not provide 100% daytime coverage of the terrestrial surface each day) and rare instances in which the atmospheric correction procedure (Vermote and Justice,

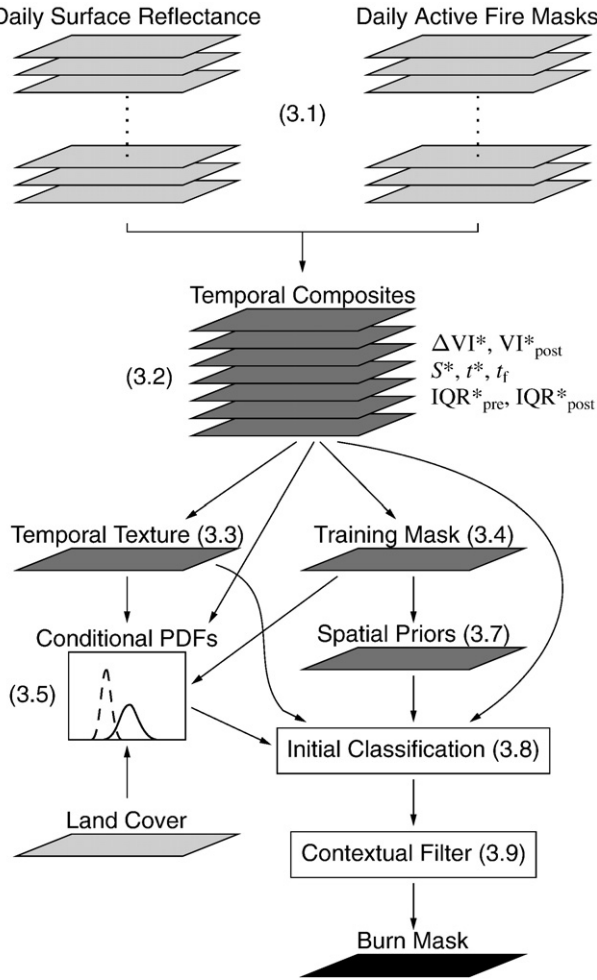


**Fig. 1.** Algorithm flow for processing individual MODIS tiles. Input data layers are shown in light grey, intermediate data layers computed internally as part of algorithm are shown in medium grey, and final output map is shown in dark gray. Numbers in parentheses refer to section numbers in main text.

2002) produces an out-of-bounds result. The daily reflectances are denoted as  $\rho_{1,i}$ ,  $\rho_{5,i}$  and  $\rho_{7,i}$ , respectively, where the index  $i$  numbers the individual days for which valid observations are available ( $i=1,2,3,\dots,N$ ). A record of the ordinal day of year from which each observation was selected is also recorded and is denoted as  $t_i$ .

In general, both the Terra and Aqua daily surface reflectance products should be used in combination to minimize gaps in the daily time series. When observations from both instruments are available, a single daily reflectance is independently selected for each grid cell by choosing the cloud-free observation sensed at the smaller view zenith angle; in this way the area sensed by the MODIS pixel on the surface and lingering bi-directional reflectance effects are minimized.

Given the daily reflectance time series for each grid cell, a daily burn-sensitive vegetation index  $VI_i$  is then computed, where

$$VI_i = \frac{\rho_{5,i} - \rho_{7,i}}{\rho_{5,i} + \rho_{7,i}}. \quad (1)$$

This ratio spectral index shows a significant decrease following a burn and provides good burned–unburned discrimination using MODIS data (Roy and Landmann, 2005). Similar indices have been found to provide comparable burned–unburned discrimination using Landsat TM bands 4 (0.83  $\mu\text{m}$ ) and 7 (2.2  $\mu\text{m}$ ) (Lopez Garcia and Caselles, 1991; Miller and Yool, 2002). An example of the behavior of

this index is illustrated in Fig. 2, which shows the daily surface reflectance and VI time series for a 500-m grid cell in northern Australia from mid-July through late November 2001. This particular grid cell burned on 28 August (ordinal day 240), causing the abrupt decrease in band 5 reflectance and accompanied by little or no immediate change in band 7 (top panel). This is followed by a period of gradually increasing reflectance due primarily to vegetation regrowth. The corresponding VI time series (center panel) shows a similar decrease associated with the burn, with noticeably longer persistence. This characteristic abrupt decrease in VI is the primary indicator used within the algorithm to identify burned areas.

### 3.2. Composite change summary

The algorithm first examines the daily VI time series by considering observations within two adjacent sliding temporal windows, each of which contain  $W=10$  successive daily observations; these windows are referred to as the *candidate pre-burn* and *candidate post-burn* windows, respectively. For our time series of  $N$  valid observations,  $N-2W+1$  such pairs of adjacent windows exist.

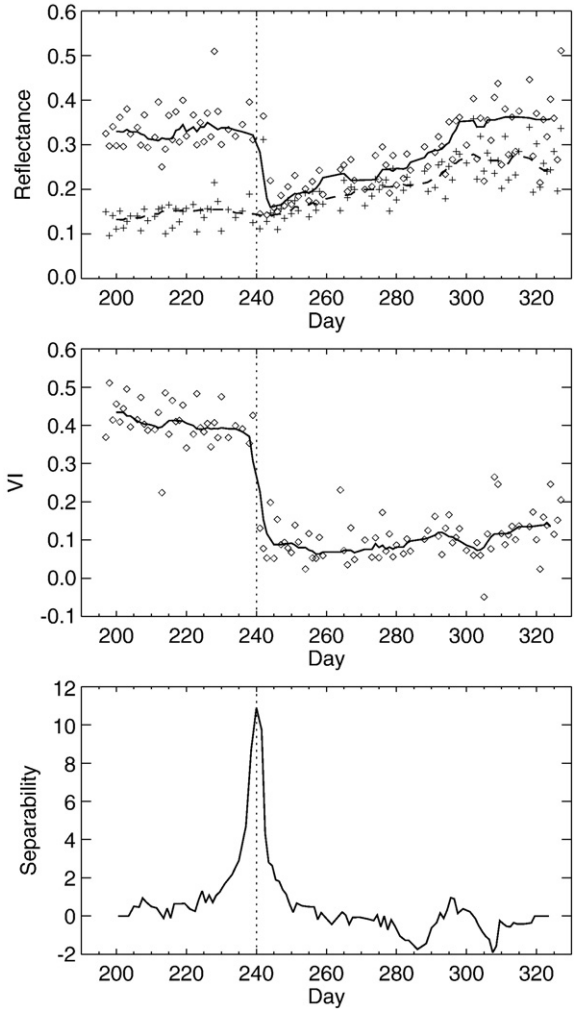


**Fig. 2.** Daily time series for a 500-m grid cell in northern Australia (MODIS tile h31v10) from mid-July through late November 2001. The grid cell is located within an area that burned on ordinal day 240 (dotted vertical line). Top panel: MODIS band 5 (diamonds) and band 7 (plus signs) reflectance time series; the lines show the series after smoothing. Center panel: Corresponding VI time series. Bottom panel: Corresponding temporal separability of VI time series calculated using Eq. (2).

We use the index  $k$  to reference the position within the daily time series in which the sliding windows are aligned ( $k=1,2,\dots,N-2W+1$ ); incrementing  $k$  moves both windows forward in time by one day.

The following VI statistics are computed for the  $k$ th pre-burn window:

$$\begin{aligned} \text{VI}_{\text{pre}}(x, y, k) &= \text{mean}(\text{VI}_i(x, y, p), i \in \{k, \dots, k+W-1\}) \\ \sigma_{\text{pre}}(x, y, k) &= \text{stdev}(\text{VI}_i(x, y, p), p) \end{aligned}$$

where mean and stdev denote the  $p$ -percent trimmed mean and standard deviation, respectively, of the observations in the window, with  $p$  nominally set to 10% (i.e., the smallest tenth and largest tenth of the observations are excluded), and  $(x, y)$  is the location of the 500-m grid cell within the MODIS tile. Statistics for the  $k$ th candidate post-burn window are similarly computed:

$$\begin{aligned} \text{VI}_{\text{post}}(x, y, k) &= \text{mean}(\text{VI}_i(x, y, p), i \in \{k+W, \dots, k+2W-1\}) \\ \sigma_{\text{post}}(x, y, k) &= \text{stdev}(\text{VI}_i(x, y, p), p). \end{aligned}$$

Grid cells having too few ( $N < 2W$ ) valid observations to fill the candidate pre- and post-burn windows are immediately labeled as *unclassified* and are subsequently ignored.

A measure of temporal separability  $S$ , defined as

$$S(x, y, k) = \frac{\Delta \text{VI}(x, y, k)}{[\sigma_{\text{pre}}(x, y, k) + \sigma_{\text{post}}(x, y, k)]/2}, \quad (2)$$

where  $\Delta \text{VI}(x, y, k) = \text{VI}_{\text{pre}}(x, y, k) - \text{VI}_{\text{post}}(x, y, k)$ , is evaluated for all  $k$ . Large, rapid decreases in the VI time series (relative to the variability in the time series) will yield large positive values of  $S$ , constant or gradually changing VI time series will yield  $S \approx 0$ , and a large, rapid increase in the VI time series will yield a negative separability of large magnitude. This behavior is illustrated in Fig. 2 (bottom panel) for the Australian time series introduced in Section 3.1.

The maximum separability within the time series is identified for each pixel, and the value of  $k$  at which this maximum occurs is designated  $k^*$ . The day associated with the maximum change,  $t^*(x, y)$ , is the midpoint of the interval between the date of the last observation in the pre-burn window and the date of the first observation in the post-burn window, i.e.,  $t^*(x, y) = (t_{k^*+W-1} + t_{k^*+W})/2$ . The interval  $\Delta t^*(x, y) = t_{k^*+W-1} - t_{k^*+W}$  is similarly computed for each pixel as it will subsequently be used to estimate the uncertainty in burn date.

The time series for each 500-m grid cell of the MODIS tile is processed in the above manner, yielding composite images of  $\Delta \text{VI}(x, y, k^*)$ ,  $\text{VI}_{\text{post}}(x, y, k^*)$ ,  $S(x, y, k^*)$ ,  $t^*(x, y)$ , and  $\Delta t^*(x, y)$ , for use in subsequent phases of the detection algorithm. To avoid having to repeatedly write the index  $k^*$ , we adopt for legibility the more concise notation  $\Delta \text{VI}^*(x, y) \equiv \Delta \text{VI}(x, y, k^*)$ ,  $\text{VI}_{\text{post}}^*(x, y) \equiv \text{VI}_{\text{post}}(x, y, k^*)$ ,  $S^*(x, y) \equiv S(x, y, k^*)$ , etc., hereafter.

Though not used in the algorithm, the changes in bands 2, 5, and 7 reflectance time series associated with  $k^*$  are recorded for diagnostic purposes. We denote these composites as  $\Delta \rho_2^*(x, y)$ ,  $\Delta \rho_5^*(x, y)$ , and  $\Delta \rho_7^*(x, y)$ , respectively. As with the daily VI time series, the daily reflectances are trimmed when computing the mean reflectance within the candidate pre- and post-burn windows.

The candidate pre- and post-burn windows will always contain a fixed number of valid observations ( $W$ ), and are therefore *variable length* windows since a valid observation will generally not be available every day (e.g., due to cloud obscuration). It is consequently important to retain information about the range of dates represented within each window, for if this interval were to become excessively large, the associated pre- and/or post-burn statistics could not reasonably be assumed to represent short-term snapshots of the time series, i.e. the windows would likely span longer-term seasonal trends. We therefore compute the interquartile range (IQR) of the dates spanned by the maximum-separability pre- and post-burn windows, denoted  $\text{IQR}_{\text{pre}}^*(x, y)$  and  $\text{IQR}_{\text{post}}^*(x, y)$ , respectively. We use

the IQR because it is a robust measure better matched to the trimmed VI statistics computed for each window. If either  $\text{IQR}_{\text{pre}}^*(x, y)$  or  $\text{IQR}_{\text{post}}^*(x, y)$  exceeds 30 days, the pixel at  $(x, y)$  is classified as *unburned* but ignored in subsequent processing until the final classification phase (Section 3.9), with the pixel's special "presumed unburned" status flagged in a separate quality assurance layer.

A cumulative mask identifying those 500-m pixels in which active fires were detected during the time period being processed is produced concurrently from the daily 1-km MOD14A1/MYD14A1 fire products replicated to 500-m resolution. In producing this mask, we retain the date on which the fire was detected, which we write as  $t_f(x, y)$ . If multiple fires were detected within the same pixel on different dates, the date nearest to  $t^*(x, y)$  is chosen.

Examples of four of the composites ( $\Delta \text{VI}^*$ ,  $\text{VI}_{\text{post}}^*$ ,  $t^*$ , and  $t_f$ ) for our Australian example tile are shown in Fig. 3. We note in passing the significant differences in  $\Delta \text{VI}^*$  (Fig. 3a) and especially  $\text{VI}_{\text{post}}^*$  (Fig. 3b) within different land cover types, and will return to this issue in Section 3.5.

### 3.3. Temporal texture

As illustrated in Fig. 3c, the day of maximum change ( $t^*$ ) shows much higher spatial coherence in areas that have burned compared to areas that have not burned. To facilitate the use of this textural information in our classification algorithm, we compute the local standard deviation of  $t^*$  within a five-pixel "rook's case" window centered about each 500-m pixel. To prevent the loss of fine, 1-pixel sections of burned patches, the texture map is filtered with an edge-restoring ranked order filter (Astola and Kuosmanen, 1997), which selects the 33rd percentile within each  $3 \times 3$  kernel (selecting the 50th percentile instead would be the equivalent of a median filter). We denote the resulting filtered temporal texture as  $\sigma_t^*$ .

### 3.4. Selection of training pixels

The cumulative active fire map described in Section 3.2 provides a useful starting point for identifying representative burned and unburned pixels that can be subsequently used to perform a supervised classification. As noted in Section 1, this identification process must be performed judiciously. To ensure that training samples are not excessively contaminated, the active fire data undergo a process of spatial and temporal "cleaning" in combination with region growing.

#### 3.4.1. A-priori unburned pixels

Selection of training pixels is initiated by identifying pixels that are very unlikely to have burned during the mapping period. The pixel at location  $(x, y)$  is identified as an unburned pixel *a priori* if either of the following conditions are satisfied:

$$S^*(x, y) < 2 \quad (3)$$

$$\sigma_t^*(x, y) > 8 \text{ days}. \quad (4)$$

These criteria are conservative absolute thresholds for identifying broad regions of high temporal heterogeneity and low VI separability, two characteristics which are extremely atypical of recent burns, and were selected empirically based on a very large sample of burns from more than 140 different MODIS tiles distributed about the globe.

#### 3.4.2. Burned training pixels

A subset of those pixels flagged in the cumulative active fire mask are used to create an initial burned training mask. The cumulative mask is first "cleaned" by morphological erosion with a  $3 \times 3$  structuring element to eliminate small clusters of active fire pixels which are less likely to be accompanied by a detectable burned area

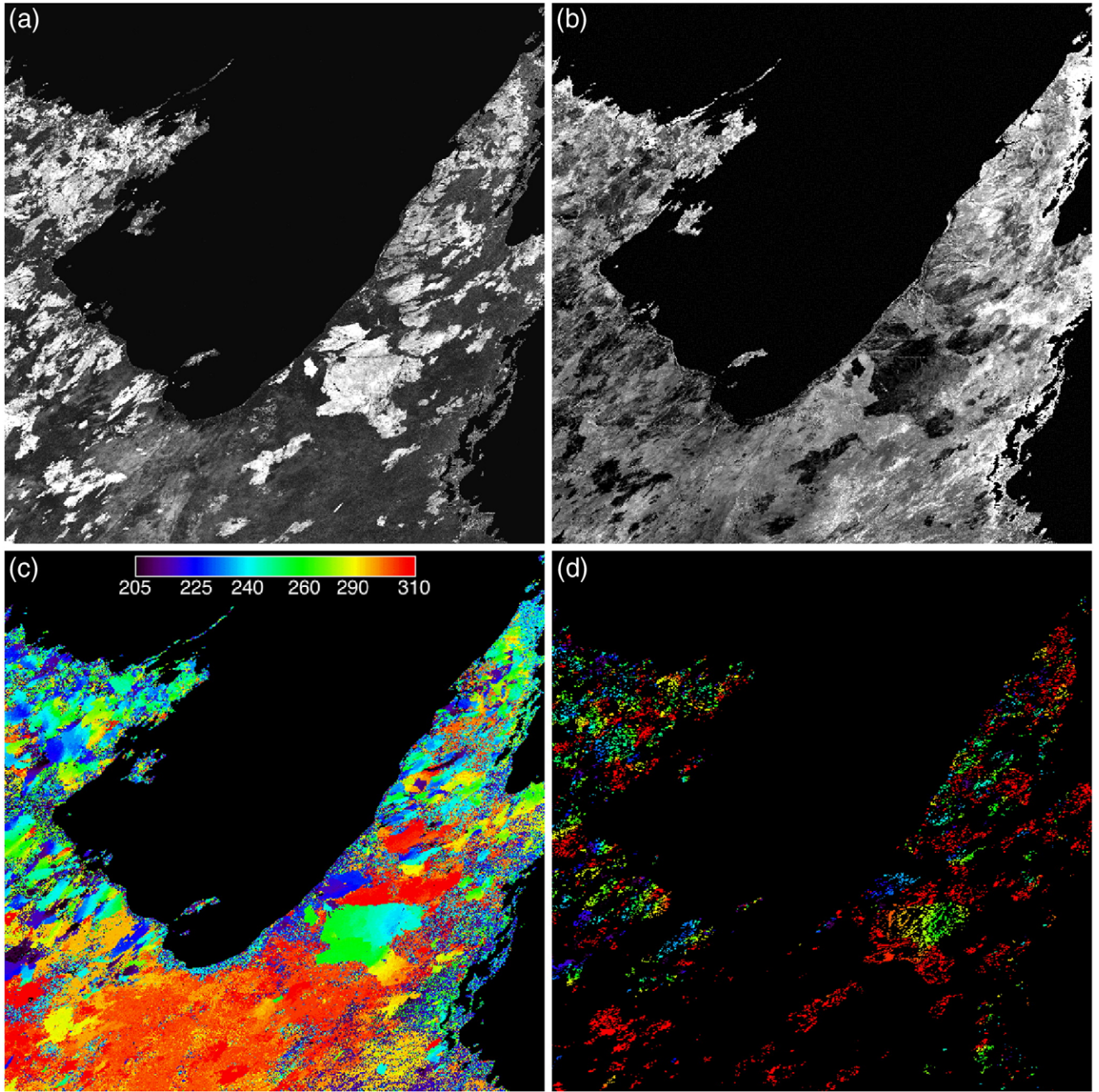


**Fig. 3.** Example of composite imagery used in detection algorithm for MODIS tile h31v10 in northern Australia, for a mapping period spanning August through October 2001. (a)  $\Delta VI^*$ , the change between pre- and post-burn VI, with lighter shades of grey representing a larger change; burn scars appear as light patches in this composite. (b)  $VI_{\text{post}}^*$ , the post-burn VI associated with day of maximum separability, with higher VI shown in lighter shades of grey; burn scars appear as dark patches in this composite. (c) Day of maximum separability ( $t^*$ ), with color encoding ordinal day of year. (d) Cumulative active fire mask ( $t_f$ ), with color indicating day on which the fire was detected, and using the same color scale as in (c).

(the edges of large clusters of fire pixels, which are less likely to have burned, are also removed in the process). A series of threshold tests is then applied to those fire pixels that remain:

$$|t_f(x,y) - t^*(x,y)| \leq \Delta t^*(x,y) + 5 \text{ days} \quad (5)$$

$$S^*(x,y) \geq 2 \quad (6)$$

$$\sigma_{t^*}(x,y) \leq 8 \text{ days}. \quad (7)$$

The eroded set of fire pixels satisfying conditions (5)–(7) form the *initial burned training mask*. Condition (5) restricts the training pixels to those in which an active fire was detected on approximately the same day as the maximum separability in the VI time series occurred.

The criteria in Eqs. (6) and (7) are the converse of the tests used to identify *a-priori* unburned pixels (Section 3.4.1).

At tropical and sub-tropical latitudes the overpass frequency of the Terra and Aqua MODIS sensors, even in combination, results in a cumulative active-fire mask that often greatly under-represents the spatial extent of large burns. To remedy the loss of potentially large numbers of training pixels in such cases, the initial burned training mask is expanded through region growing. Individual clusters of fire pixels, which will serve as the initial seeds, are identified within the initial burned training mask, and various statistics (discussed below) are computed for each cluster. Each cluster is then iteratively grown in turn, provided it is at least some minimum number of pixels (nominally 50) in size. During each iteration, all valid pixels adjacent

to any seed pixel associated with the  $j$ th cluster, and which were not identified as *a priori* unburned pixels (Section 3.4.1), are candidates for addition to the cluster. Adopting the notation  $\Delta\text{VI}^*(j)$  and  $\text{VI}_{\text{post}}^*(j)$  to denote the values of  $\Delta\text{VI}^*$  and  $\text{VI}_{\text{post}}^*$ , respectively, for all pixels within the  $j$ th *initial* cluster, the candidate pixel at  $(x, y)$  is added to the cluster if it satisfies the following conditions:

$$\Delta\text{VI}^*(x, y) > 25\text{th percentile of } \Delta\text{VI}^*\{j\} \quad (8)$$

$$\text{VI}_{\text{post}}^*(x, y) < 75\text{th percentile of } \text{VI}_{\text{post}}^*\{j\} \quad (9)$$

$$\sigma_t^*(x, y) \leq 3 \text{ days} \quad (10)$$

$$d_l(x, y) \leq R_g, \quad (11)$$

where  $d_l(x, y)$  denotes the distance from the candidate pixel to the nearest burned training pixel in the initial burned training mask, and the constant  $R_g$  is the *maximum growing radius* with a fixed value of 10 km. The criteria in conditions (8) and (9) require that  $\Delta\text{VI}^*$  and  $\text{VI}_{\text{post}}^*$  observed for a new seed resemble the more-obviously-burned fraction of the burned training pixels comprising the initial cluster. Condition (10) is a highly conservative threshold for identifying regions of nearly-coincident temporal change characteristic of burned areas. Condition (11) helps ensure that our (local) cluster statistics are only applied locally, and prevents runaway region growing.

In adding a candidate pixel to a cluster, it is labeled as a burned training pixel as well as a new seed to be used in the subsequent iteration. Iterations are continued until no new seed pixels are identified, at which point the next cluster is grown, until all clusters have been processed. Note that while the initial clusters will always be distinct, it is possible for a candidate burned training pixel to be agglomerated into multiple clusters.

#### 3.4.3. Unburned training pixels

In producing a complementary mask of unburned training pixels, we exploit information from *a priori* unburned pixels as well as the burned training mask. Adopting the notation  $d_B(x, y)$  to mean the distance from location  $(x, y)$  to the nearest burned training pixel, the pixel at location  $(x, y)$  is flagged as an unburned training pixel if either of the following conditions are satisfied: 1) the pixel is an *a priori* unburned pixel, or 2) the pixel contains valid data, is not a burned training pixel, and has  $d_B(x, y) > R_d$ , where the parameter  $R_d = 5$  km. Pixels in the second category are efficiently identified by dilating the burned training mask with an elliptical structuring element having the proper size and orientation to compensate for the spatial distortion introduced by the MODIS sinusoidal projection. The final training mask for our Australian example tile is shown in Fig. 4.

In much of Africa, particularly the Sahel, even relatively small flaming fronts can burn extensive areas of herbaceous vegetation very quickly. This can exacerbate the undersampling of burned areas in the cumulative active fire mask, producing an excess of tiny fire-pixel clusters that are too small to serve as seeds during the region growing phase. To help recover burned training pixels, the dilation radius  $R_d$  is increased to 10 km for tiles in Africa. The dilation radius is further increased to 20 km during the Terra-only period prior to July 2002.

#### 3.5. Extraction of conditional probability densities

Given the masks of burned and unburned training pixels produced in the previous step, we now derive the conditional probability density functions (PDFs)  $P_l(\Delta\text{VI}^*|B)$  and  $P_l(\Delta\text{VI}^*|U)$ , where “B” and “U” denote the classes *burned* and *unburned*, respectively, for each land cover class  $l$  present in the MODIS tile; we use the Hansen et al. (2000) classification scheme available in the MODIS land cover product. (The rationale for this stratification will be explained shortly.) In producing

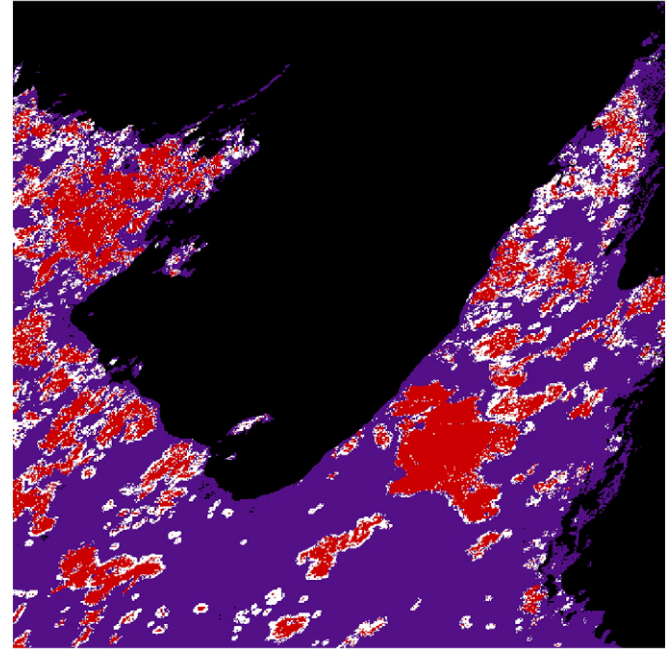


**Fig. 4.** Training mask for the Australian example of Fig. 3 used to guide extraction of conditional probability distributions and selection of spatial prior probabilities. Water and missing-data pixels are shown in black, unburned training pixels are shown in purple, burned training pixels are shown in red, and the remaining pixels not used for training are shown in white.

these distributions we use a Gaussian kernel density estimator  $P(x)$  with standard deviation  $\sigma_k = 0.02$ , where

$$P(u) = C \sum_i \exp\left(-\frac{|u - u_i|^2}{2\sigma_k^2}\right) \quad (12)$$

and the summation is taken over each pixel in the training sample. The constant  $C$  is a normalization factor which ensures that the integral of  $P$  over all  $u$  is 1. In a similar manner, the conditional probability densities  $P_l(\text{VI}_{\text{post}}^*|B)$  and  $P_l(\sigma_t^*|B)$  are computed (for these variables the conditional unburned PDFs are not needed).

Examples of the conditional PDFs  $P_l(\Delta\text{VI}^*|B)$  and  $P_l(\Delta\text{VI}^*|U)$  for the woody savanna land cover class within our example Australian tile are shown in Fig. 5a. The corresponding burned PDFs  $P_l(\Delta\text{VI}_{\text{post}}^*|B)$  and  $P_l(\sigma_t^*|B)$  are shown in Fig. 5b and c, respectively. For comparative purposes the conditional unburned PDFs  $P_l(\text{VI}_{\text{post}}^*|U)$  and  $P_l(\sigma_t^*|U)$  are also shown, but are not actually used within the algorithm. The reason for this is because both  $\text{VI}_{\text{post}}^*$  and  $\sigma_t^*$  can be strongly affected by old burns which predate the mapping period, thus alone these variables cannot guarantee that a burn was recent. In contrast,  $\Delta\text{VI}^*$  captures only those burns that occurred during the mapping period, and is therefore more useful as it is only recent burns that are the objective of the algorithm.

The rationale for isolating separate PDFs within individual land cover classes is to help account for differences in vegetation phenology, fuel state (e.g., structure and moisture content), and fire conditions (e.g., head fire vs. back fire), which are all factors that determine the signal ultimately recorded by the sensor. In Fig. 6 we show an example of the differences in the PDFs for different land cover classes, again from the Australian case first presented in Fig. 3.

#### 3.6. Separability test

The burned and unburned  $\Delta\text{VI}$  probability distributions for each land cover class are next tested to ensure that they are sufficiently different to permit burned and unburned pixels to be discriminated.

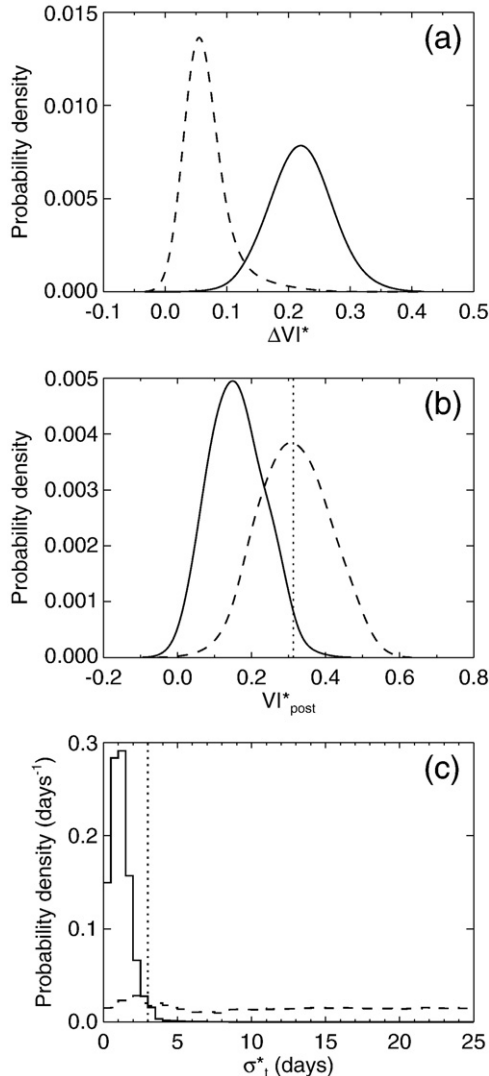


**Fig. 5.** Burned (solid line) and unburned (dashed line) conditional probability density functions derived from training pixels within the woody savanna land cover class in the Australian MODIS tile. (a) PDFs for  $\Delta VI^*$ . (b) PDFs for  $VI^{*}_{post}$ , with the dotted vertical line indicating the 98th percentile of the burned distribution. (c) PDFs for  $\sigma_t^*$  (temporal texture), with the dotted vertical line again indicating the 98th percentile of the burned distribution.

As our measure of separability we use the Hellinger distance,  $H$ , which for probability densities  $P_1(u)$  and  $P_2(u)$  is defined as (Upton and Cook, 2002)

$$H(P_1, P_2) = \left[ 2 \left( 1 - \int_{-\infty}^{+\infty} \sqrt{P_1(u)P_2(u)} du \right) \right]^{1/2}, \quad (13)$$

where  $0 \leq H \leq \sqrt{2}$ , with  $H=0$  indicating that the distributions are identical (i.e., completely inseparable) and  $H=\sqrt{2}$  indicating that the distributions have no overlap whatsoever. If  $H(P_l(\Delta VI^*|B), P_l(\Delta VI^*|U)) < 0.4$  for land cover class  $l$ , all pixels belonging to this land cover class are immediately classified as *unburned*, and processing continues for the remaining land cover classes present in the MODIS tile.

In rare cases it is possible for the burned and unburned PDFs to exceed this minimum separability criterion, yet to exhibit sufficient overlap that the majority of the burned and unburned training samples share essentially the same parent distribution. This can occur when the number of burned training pixels is small, resulting in a poor statistical sample. Under these circumstances, the right tail of the

unburned distribution can potentially extend beyond the right tail of the burned distribution, inflating  $H$ . To guard against this situation, we check if the 95th percentile of  $P_l(\Delta VI^*|B)$  is less than or equal to the 95th percentile of  $P_l(\Delta VI^*|U)$ . If so, all pixels within the current land cover class are classified as *unburned* in the same manner as described above.

### 3.7. Posterior burned probability

The probability of a grid cell within land cover class  $l$  having burned during the compositing period given the observed change in VI is estimated using Bayes' rule:

$$P(B|\Delta VI^*(x, y)) = \frac{P_l(\Delta VI^*|B)P_B(x, y)}{P_l(\Delta VI^*|B)P_B(x, y) + P_l(\Delta VI^*|U)P_U(x, y)} \quad (14)$$

where "B" and "U" denote the classes *burned* and *unburned*, respectively. The prior probabilities  $P_B(x, y)$  and  $P_U(x, y)$  are set independently for each 500-m pixel using the following simple scheme: If the pixel was identified as a burned training pixel (Section 3.4.2),  $P_B$  is assigned a value of  $P_{max}=0.5$ , reflecting the much higher likelihood that the pixel in fact burned. If the pixel was identified as an *a priori* unburned training pixel,  $P_B$  is assumed to be zero. If the pixel is neither a burned training pixel nor an unburned training pixel, the prior probability is computed as a function of its proximity to the nearest burned training pixel using the Gaussian weighting function

$$P_B(x, y) = (P_{max}-P_{min}) \times \exp\left(-\frac{d_B^2}{2\sigma_p^2}\right) + P_{min}, \quad (15)$$

where as before  $d_B(x, y)$  is the distance from  $(x, y)$  to the nearest burned training pixel,  $\sigma_p=5$  km (established empirically), and  $P_{min}=0.02$ . (For tiles in Africa,  $P_{min}=0.05$  for reasons discussed in Section 3.4.3). Given the burned prior probability, the prior probability of a pixel having not burned is then  $P_U(x, y)=1-P_B(x, y)$ .

The spatially varying probability in Eq. (15) is merely a way (albeit an arbitrary one) of expressing our prior expectation that burns are more likely to occur near other burns. As  $d_B$  increases, the prior probability decreases, asymptotically converging toward a minimum of  $P_{min}$ . The comparatively small value specified for  $P_{min}$  reflects the fact that within most MODIS tiles a randomly selected 500-m grid cell is very unlikely to have recently burned.

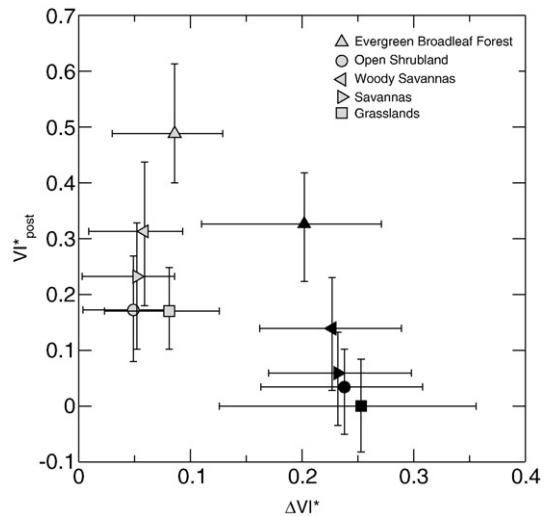


**Fig. 6.** Median  $VI^{*}_{post}$  vs. median  $\Delta VI^*$  for unburned (light grey symbols) and burned (black symbols) training samples associated with each land cover class in the Australian example of Fig. 3. Error bars indicate 10th and 90th percentiles of each distribution.

### 3.8. Initial classification

During this phase the algorithm produces an initial classification of *burned* or *unburned* for each valid 500-m pixel within the MODIS tile. A separate missing-data class is assigned to water pixels as well as those lacking valid data. In preparation for this initial classification, two relative thresholds are computed for each land cover class: 1) the 98th percentile of  $P_l(VI_{post}^*|B)$ , denoted  $Q_l^{(98)}(VI_{post}^*|B)$  (see Figs. 5b; and 2) the 98th percentile for  $\sigma_t^*$ , denoted  $Q_l^{(98)}(\sigma_t^*|B)$  (see Fig. 5c). Both thresholds will be used to identify “outliers” near (or beyond) the upper limits of the respective burned distributions that bear the greatest resemblance to unburned pixels. Pixels satisfying the following criteria are labeled as *burned*:

- (1) The pixel was not identified as an *a priori* unburned pixel during selection of training pixels (Section 3.4.1);
- (2) the posterior probability  $P(B|\Delta VI^*(x, y))$  is at least 0.6, a threshold empirically determined to keep the frequency of commission errors very low;
- (3)  $VI_{post}^*(x, y) \leq Q_l^{(98)}(VI_{post}^*|B)$ ;
- (4)  $\sigma_t^*(x, y) \leq Q_l^{(98)}(\sigma_t^*|B)$ .

Pixels that fail to satisfy any of the above criteria are classified as *unburned*.

### 3.9. Final classification

In this final step contextual information is used to refine the initial classification. The original prototype algorithm used the iterated conditional modes (ICM) method (Besag, 1986) with a simple Markov random field model for this purpose. Subsequent tests demonstrated that, in this application, one-pass filters could provide comparable performance with far less computational effort, and a modified majority filter was selected to replace the original scheme. The revised approach considers  $n_B$ , the number of temporally-consistent burned pixels among the eight adjacent neighbors (“queen’s case”) surrounding the pixel being processed. Pixels at adjacent locations  $(x, y)$  and  $(x', y')$  are considered to be temporally consistent if  $|t^*(x, y) - t^*(x', y')| \leq 5$  days. If the candidate pixel was initially labeled *burned* and  $n_B < 3$ , it is relabeled *unburned*. If the candidate pixel was initially labeled *unburned* and  $n_B \geq 6$ , it is relabeled *burned*.

The final classification for our Australian example tile is shown in Fig. 7. In this case about 0.5% of all land pixels within the tile were relabeled during the final contextual filtering phase.

## 4. Accuracy assessment

We assessed the accuracy of the burned area maps produced with our algorithm in three different regions (Fig. 8). Reference burned area data for each region was compiled using high resolution Landsat imagery. The regions span a variety of biomes, including middle taiga in central Siberia, temperate forests, shrublands, and grasslands in the United States, and African grass savannas and Miombo woodland. These ecosystems differ in ecological setting, fuel loading, and fire regime, and thus present a diverse sample of conditions for algorithm evaluation.

We performed two types of accuracy assessment within each of the study areas: an *inventory accuracy assessment*, to evaluate the ability of the algorithm to estimate sizes of individual burned areas, and a *geographic accuracy assessment*, to evaluate the spatial fidelity of mapping on a per-pixel basis.

### 4.1. Central Siberia

The central Siberian study region spans an area of ~50 Mha for which we used 18 Landsat ETM+ scenes acquired between 17 July 2001 and 19 August 2002. These scenes are distributed across dense

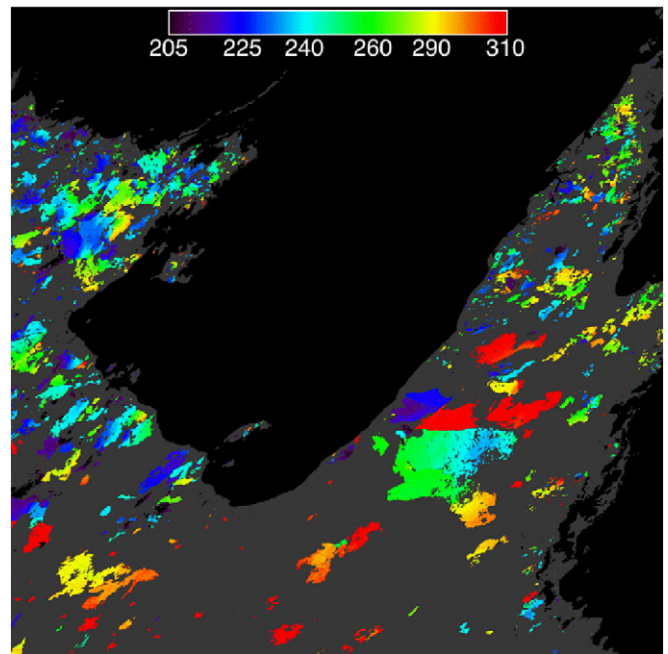


**Fig. 7.** Final burn scar mask for the Australian example of Fig. 3, using the same color scheme to encode the burn date.

evergreen (pine) and deciduous (larch) needleleaf forests in the central section, sparse larch-dominated forests and open woodlands in the eastern section, and a mixture of larch-dominated and mixed forest in the western section of the study area (Fig. 8a). Large fires occur within this area on an annual basis (Ivanova and Ivanov, 1999). Subsequently, we were able to collect a large sample ( $N=649$ ) of burned areas ranging from approximately 5 to 320,000 ha in size mapped in the ETM+ imagery, aggregated to 100-m to account for modulation transfer function effects amplified by the presence of smoke in scenes with ongoing burning. A description of the Landsat-based burned area data set is provided in Loboda et al. (2007).

The inventory assessment (Fig. 9a) showed that in this region the MODIS burned area maps slightly underestimate the true burned area (slope = 0.913, intercept = -55 ha, with coefficient of determination  $r^2 = 0.989$ ). In addition, the algorithm mapped the spatial distribution of the burns in this region reasonably well with an overall kappa coefficient (Congalton and Green, 1999) for all scenes combined of 0.79 and an accuracy of 98.4% (Table 1).

### 4.2. United States

The United States study area is the most ecologically diverse of the study areas in the accuracy assessment. It consists of burned areas located in the humid Florida coastal plain, semi-arid basins, plateaus and ranges in the interior west, the eastern Sierra Nevadas, and the Mediterranean southern California coast (McNab et al., 2007). General vegetation cover types for each of these regions is based on McNab et al. (2007) and includes evergreen southern pine forests in the Florida coastal plain; low biomass shrublands and grasslands in the basins and plateaus of the Great Basin shifting to conifer woodlands and forests at higher elevations in adjacent mountain ranges; shrublands, conifer woodlands and forests of the eastern Sierra Nevadas; and, chaparral shrublands and oak woodlands of the southern California coastal areas shifting to evergreen forests on adjacent inland mountains. These areas facilitate the evaluation of MODIS burned area maps for grassland, shrubland, woodland and forested fires in a variety of ecological settings.

We used seven Landsat TM/ETM+ scene-pairs (14 scenes in total) to obtain representative pre- and post-fire reflectance imagery

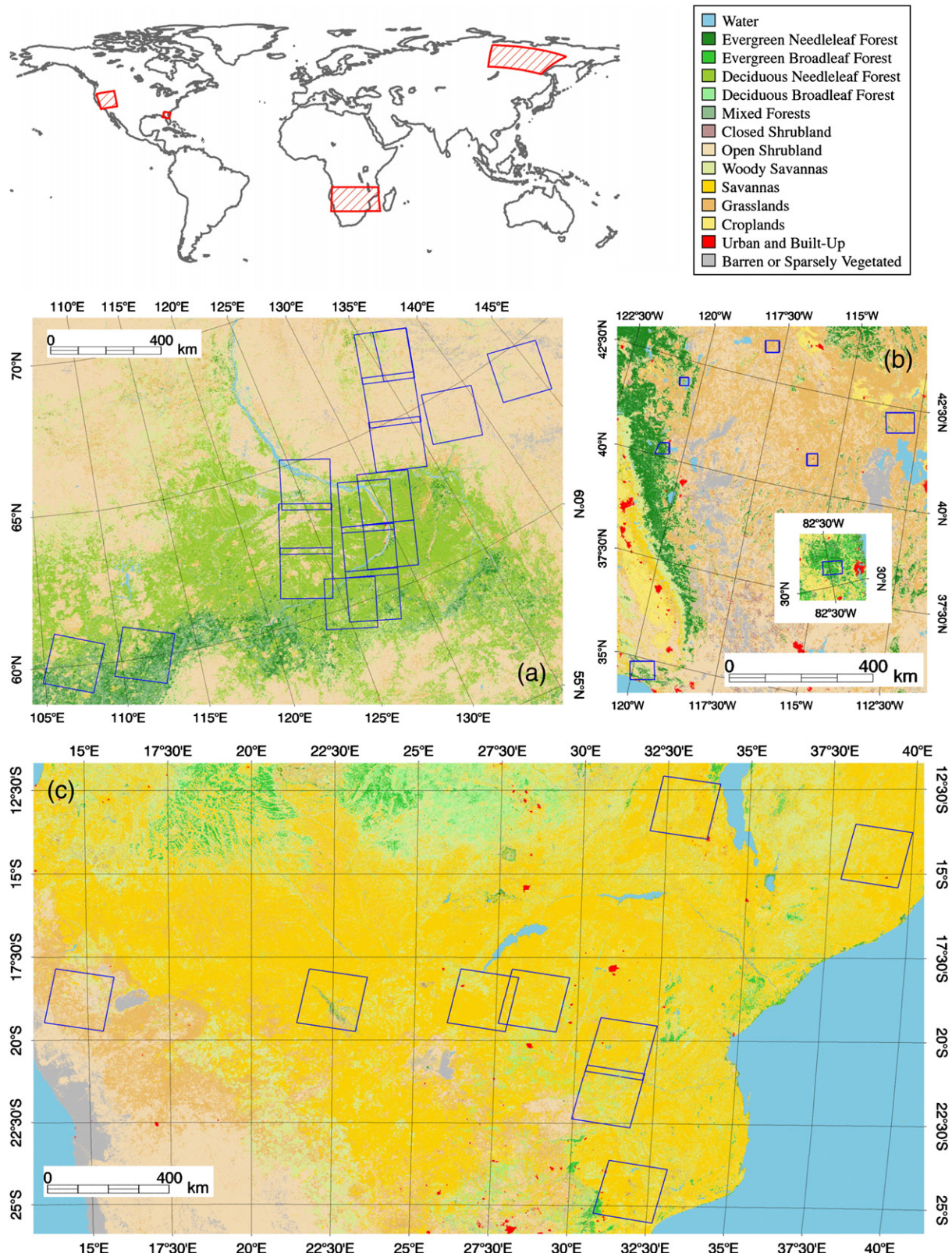


**Fig. 8.** Locations of Landsat scenes (outlined in dark blue) used for validation, superimposed on the Hansen et al. (2000) land cover class from the MODIS land cover product. The red boxes in the global map (upper left panel) show the spatial extent of each regional map. (a) Central Siberia. (b) Western United States, with additional site in northern Florida (map inset). (c) Southern Africa.

corresponding to fire activity that occurred within the scene between 2004 and 2007 (Fig. 8b). Pre- and post-fire Normalized Burn Ratio (NBR) data were compiled at the native 30-m spatial resolution of the

Landsat imagery. Each of the seven bi-temporal NBR pairs was difference and thresholded to extract the burned areas for each sampled scene (Key and Benson, 2006). We identified a total of 26

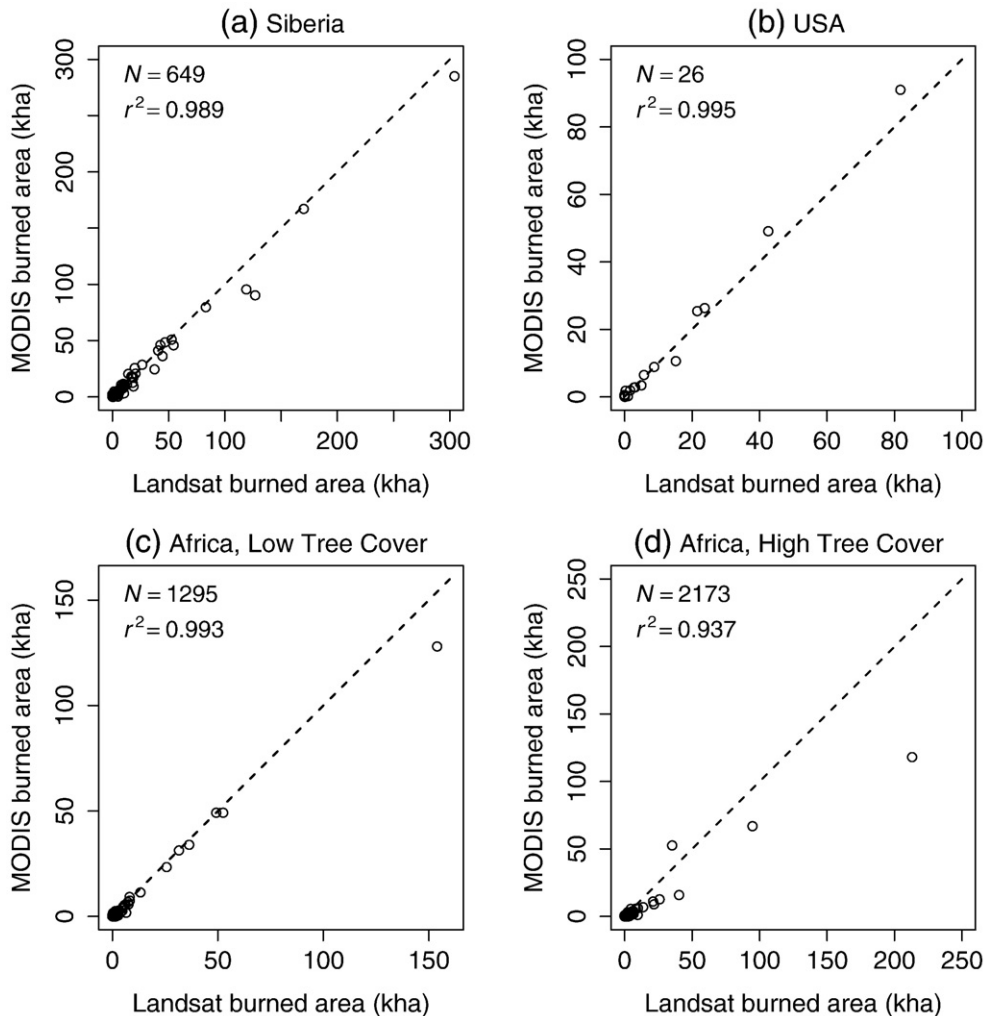


**Fig. 9.** Areas of individual burn scars mapped by the 500-m burned area detection algorithm versus ground truth derived manually from 30-m Landsat imagery. Shown for each plot are the number of burn scars,  $N$ , and the square of the linear correlation coefficient,  $r^2$ , or the “coefficient of determination”. (a) Results for Siberia during 2001 and 2002 burning seasons. (b) Results for the (primarily) western USA. (c) and (d) Results for southern Africa during the 2002 burning season, with burn scars partitioned into low (below 21%) and high (21% or higher) fractional tree cover. Dashed 1:1 line indicates perfect agreement.

burned areas for all seven scenes ranging from approximately 0.1 ha to 82,000 ha in size. Available burned area data compiled by the Monitoring Trends in Burn Severity (MTBS) Project (Eidenshink et al., 2007) were also used verify the location and extent of delineated burned areas.

The inventory assessment (Fig. 9b) showed that in this region the MODIS burned area maps overestimate the true burned area by approximately 12% (slope = 1.12, intercept = -262 ha, with  $r^2 = 0.995$ ). Results of the geographic accuracy assessment are shown in Table 1, with  $\kappa = 0.82$  and an overall accuracy of 94.8%.

#### 4.3. Southern Africa

We used nine Landsat ETM+ scene-pairs (18 scenes in total) acquired during the 2002 dry season distributed geographically to encompass representative sub-continental variation in burned area characteristics and pre- and post-fire samples of both savanna and woodland fires (Fig. 8c). The Landsat burned area maps were produced by interpreting multi-temporal ETM+ imagery to map the location and approximate date of burning based upon visual comparison of the ETM+ near-infrared and short-wave infrared bands, augmented by the ETM+ thermal band and a spectral index that is sensitive to burned

vegetation (Roy et al., 2005a). Since algorithm performance was strongly dependent upon the fraction of woody vegetation for this region, we partitioned individual burns into low (<21%) and high ( $\geq 21\%$ ) mean percent tree cover subsets using the 500-m MODIS Vegetation Continuous Fields (VCF) product (Hansen et al., 2003). Results of the inventory assessment are shown in Fig. 9c and d, respectively. Of the two subsets, the low-tree-cover MODIS burn maps show better agreement with the Landsat maps, underestimating the area burned by approximately 14% (slope = 0.863, intercept = -69 ha,  $r^2 = 0.993$ ). Clearly, however, the least squares regression is driven by the single large 154-kha outlier. If this point is excluded the MODIS burned area maps fare noticeably better, with an average underestimation of only 5% (slope = 0.949, intercept = -96 ha,  $r^2 = 0.990$ ). In contrast, the high-tree-cover MODIS burn maps underestimate the area burned by 41% (slope = 0.589, intercept = -56 ha,  $r^2 = 0.937$ ). This may be because the majority of fires in southern Africa are surface fires, which may be obscured by overstory vegetation, as well as lower combustion completeness of woody biomass. Modelling suggests that understory ground fires can be sensed under certain conditions at reflective wavelengths (Pereira et al., 2004), but at present the degree to which understory fires can be detected over a range of tree cover in practice remains unknown. Results of the geographic accuracy

**Table 1**

Regional confusion matrices and kappa coefficient ( $\kappa$ ) from geographic accuracy assessment, made by resampling the 500-m MODIS burned area maps to the spatial resolution of the Landsat validation imagery

MODIS	Landsat		Producer's accuracy
	Burned	Unburned	
<i>Central Siberia (<math>\kappa=0.79</math>)</i>			
Burned	1,240,446	229,520	84.4%
Unburned	410,636	38,855,469	99.0%
User's accuracy	75.1%	99.4%	
<i>United States (<math>\kappa=0.82</math>)</i>			
Burned	2,100,997	476,302	81.5%
Unburned	269,566	11,444,905	97.7%
User's accuracy	88.6%	96.0%	
<i>Southern Africa, low tree cover (<math>\kappa=0.67</math>)</i>			
Burned	4,164,366	603,563	87.3%
Unburned	3,280,477	14,134,005	97.7%
User's accuracy	55.9%	99.6%	
<i>Southern Africa, high tree cover (<math>\kappa=0.49</math>)</i>			
Burned	4,294,323	1,070,265	80.0%
Unburned	6,697,724	81,150,886	92.4%
User's accuracy	39.1%	98.7%	

Non-percentage table entries indicate number of 30-m pixels (100-m for central Siberia).

assessment are shown in Table 1, with  $\kappa=0.67$  (overall accuracy 97.4%) and  $\kappa=0.49$  (overall accuracy 91.7%) for the low- and high-tree-cover subsets, respectively.

## 5. Suitability of vegetation index

A fundamental algorithm assumption is that the vegetation index in Eq. (1) will decrease as a result of a burn. This is potentially problematic as the post-burn reflectance in any given band will depend on the particular mixture of char, mineral ash, exposed soil, and unburned vegetation within a pixel; wind and precipitation can further alter the post-burn signal. A broad range of post-fire reflectances are consequently possible, raising the possibility that in some cases the vegetation index employed here will not necessarily behave consistently (i.e., drop) following a fire (Trigg and Flasse, 2000; Roy and Landmann, 2005; Smith and Wooster, 2005).

To explore this possibility we examined the change in band 5 and band 7 reflectance using burned areas identified manually in a comprehensive sample of MODIS tiles (here we relied on manual identification to avoid the possibility of a bias in the algorithm favoring burns for which the VI decreased). We found that while there were no universal trends in either the band 5 or the band 7 reflectance due to burning—not even the sign of  $\Delta\rho_5^*$  or  $\Delta\rho_7^*$  behaved consistently—the VI always decreased, i.e.,  $\Delta\text{VI}^*$  was always positive for burned pixels. This is illustrated in Fig. 10, which shows the change in band 5 reflectance as a function of the corresponding change in band 7 reflectance for burn scars from two representative regions. (In the figure we have plotted the median of  $\Delta\rho_5^*$  and  $\Delta\rho_7^*$  for the 500-m pixels within individual burned areas to reduce the number of points from an impractical quarter million to several thousand.) In both cases the corresponding change in VI ( $\Delta\text{VI}^*$ , not shown) remains positive. The first example (Fig. 10a) is from central Africa for January and February 2002. The strictly positive values of  $\Delta\rho_5^*$  (meaning that the band 5 reflectance decreased) are characteristic of most regions and are generally the rule in Africa. The second example (Fig. 10b) is from a tile in northwestern Australia for April through June 2003. In this case a significant subset (about 19%) of burned areas show an increase in band 5 reflectance following the burn. On a global scale this behavior is less common than the behavior shown in the African example, but is not unusual in Australia, North and South America, and Southeast Asia.

## 6. Algorithm limitations

As with any remote sensing methodology, our algorithm has limitations which ultimately dictate the suitability of the final burned area maps for specific applications. Here we discuss the most important of these limitations.

### 6.1. Errors of omission

Obscuration by tree canopy can dilute the post-burn, top-of-atmosphere radiometric signal of burns from surface fires to the extent that they are undetectable, resulting in an omission error. In addition, regions prone to persistent cloud cover can suffer from significant errors of omission, particularly in areas of rapid post-fire vegetation regrowth. Finally, the 500-m native resolution of the MODIS SWIR bands obviously constrains the size of the smallest burn that can be detected. The minimum detectable burned area can reasonably be assumed to be about one half pixel, which for a native 500-m MODIS swath pixel would correspond to an area of approximately 13 ha at

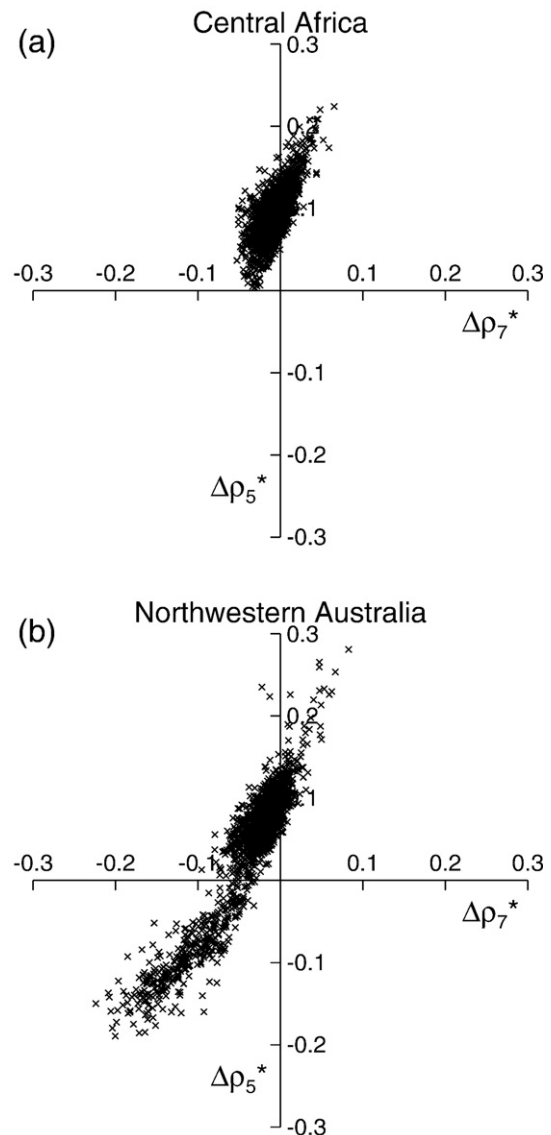


**Fig. 10.** Median change in band 5 reflectance ( $\Delta\rho_5^*$ ) versus median change in band 7 reflectance ( $\Delta\rho_7^*$ ) associated with maximum VI separability for individual burn scars in two representative regions. In both cases the corresponding change in VI ( $\Delta\text{VI}^*$ ), which is not shown, is positive. (a) Central Africa (MODIS tile h19v08), for January and February 2002. (b) Northwestern Australia (MODIS tile h30v10), from April through June 2003.

nadir. However, given the growth in pixel size at larger view angles combined with resampling errors incurred in projecting pixels onto the MODIS sinusoidal grid, this minimum will increase by roughly a factor of three. Furthermore, to avoid elimination during the final contextual filtering step a burned patch must be at least approximately three times larger still, hence the minimum detectable burn size is in the neighborhood of 120 ha. This is very much larger than the typical size of agricultural waste and deforestation burns (Giglio et al., 2006; McCarty et al., 2007), hence our mapping algorithm is not expected to reliably capture these types of burned areas.

## 6.2. Errors of commission

We have chosen values for the various algorithm parameters such that commission errors (false alarms) are generally rare. One exception occurs in regions of the tropics undergoing deforestation, where the algorithm can confuse recently cleared, unburned forest patches with burned areas. This confusion arises from similarities in spectral characteristics as well as temporal texture, and is further compounded when, as is often the case, the deforestation slash is piled within the clearing and subsequently burned after a short drying period. Under these circumstances the algorithm will often map an unpredictable fraction of the surrounding recently-cleared area as burned.

## 7. Conclusions

We have presented an automated algorithm for mapping post-fire burned areas using 500-m MODIS imagery coupled with 1-km MODIS active fire observations. The hybrid algorithm applies dynamic thresholds to composite imagery generated from a burn-sensitive vegetation index derived from MODIS channels 5 and 7, and a measure of temporal texture. Cumulative active fire maps are used to guide the selection of burned and unburned training samples and to guide the specification of prior probabilities. The combined use of active-fire and reflectance data enables the algorithm to adapt regionally over a wide range of pre- and post-burn conditions and across multiple ecosystems.

We assessed the accuracy of the burned area maps produced with our algorithm using high resolution Landsat imagery in three different regions. Mapped burned areas were accurate to within approximately 10% in all regions except higher tree-cover areas of southern Africa, where the MODIS maps underestimated the area burned by 41%. This underestimation may be due to obscuration of surface burns by overstory vegetation as well as lower combustion completeness of woody biomass.

The burned area mapping algorithm presented here uses MODIS active fire data as the source of active fire information. Aside from the MODIS fire products being in continuous production and readily available, the MODIS sensors usually have sufficient spatial resolution and temporal sampling to provide reliable burned and unburned training samples. Moreover, the local overpass times of the Terra and Aqua satellites are generally adequate for sampling the prominent diurnal fire cycle (Giglio, 2007). In principle, active fire observations from other sensors could supplement or replace the MODIS active fire data used here; the algorithm consequently provides a potential mechanism for the fusion of multi-sensor active fire observations. In practice, neither the VIRS, nor especially the ATSR sensors afford sufficient temporal sampling for their respective fire products to serve as a substitute for MODIS, although the forthcoming suite of VIIRS sensors should offer essentially a “drop-in” replacement.

The MODIS burned area product (“MCD45A1”), which is now being produced for the first time within the Collection 5 reprocessing, adopts a different, reflectance-only approach that does not exploit active fire information. As the individual MODIS land products have matured so has the feasibility of exploiting their synergy. Combining

active fire information within the burned area mapping approach as described in this paper takes advantage of the different types of fire information available from the MODIS sensor (Justice et al., 2002). This new approach is well suited to direct readout application and the code is currently being adapted for ground station use. Based in part on the success of this hybrid approach, inclusion of active fire information in the burned area mapping is planned for the MODIS Collection 6 burned area product.

## Acknowledgements

We thank Jacques Descloitres and Jacqueline Kendall (SSAI), Kelley J. O’Neal, Ivan Csiszar, Simon Trigg, Douglas Morton, Wilfrid Schroeder, and Stefania Korontzi (University of Maryland) for useful technical discussions, and four anonymous reviewers for their helpful comments and suggestions.

## References

- Arino, O., & Rosaz, J.-M. (1999, June). 1997 and 1998 world ATSR fire atlas using ERS-2 ATSR-2 data. In L. F. Neuenschwander, K. C. Ryan & G. E. Gollberg (Eds.), *Proceedings of the Joint Fire Science Conference and Workshop, Vol. 1*. (pp. 177–182). Boise, Idaho: University of Idaho and the International Association of Wildland Fire.
- Astola, J., & Kuosmanen, P. (1997). *Fundamentals of nonlinear digital filtering*. Boca Raton: CRC Press.
- Barbosa, P. M., Grégoire, J.-M., & Pereira, J. M. C. (1999). An algorithm for extracting burned areas from time series of AVHRR GAC data applied at a continental scale. *Remote Sensing of Environment*, 69, 253–263.
- Besag, J. E. (1986). On the statistical analysis of dirty pictures. *Journal of the Royal Statistical Society, Series B*, 48, 259–302.
- Congalton, R. G., & Green, K. (1999). *Assessing the accuracy of remote sensing data: Principles and practices*. Boca Raton: Lewis.
- Dozier, J. (1981). A method for satellite identification of surface temperature fields of subpixel resolution. *Remote Sensing of Environment*, 11, 221–229.
- Eidenshink, J., Schwind, B., Brewer, K., Zhu, Z., Quayle, B., & Howard, S. (2007). A project for monitoring trends in burn severity. *Fire Ecology*, 3(1), 3–21.
- Elvidge, C. D., Kroehl, H. W., Kihn, E. A., Baugh, K. E., Davis, E. R., & Hao, W.-M. (1996). Algorithm for the retrieval of fire pixels from DMSP operational linescan system data. In J. S. Levine (Ed.), *Biomass burning and global change: Remote sensing, modeling and inventory development, and biomass burning in Africa*, Vol. 1. (pp. 73–85). Cambridge: MIT Press.
- Eva, H., & Lambin, E. F. (1998). Burnt area mapping in Central Africa using ATSR data. *International Journal of Remote Sensing*, 19, 3473–3497.
- Eva, H., & Lambin, E. F. (1998). Remote sensing of biomass burning in tropical regions: Sampling issues and multisensor approach. *Remote Sensing of Environment*, 64, 292–315.
- Fernández, A., Illera, P., & Casanova, J. L. (1997). Automatic mapping of surfaces affected by forest fires in Spain using AVHRR NDVI composite image data. *Remote Sensing of Environment*, 60, 153–162.
- Fraser, R. H., Fernandes, R., & Latifovic, R. (2003). Multi-temporal mapping of burned forest over Canada using satellite-based change metrics. *Geocarto International*, 18(2), 37–47.
- Fraser, R. H., Li, Z., & Cihlar, J. (2000). Hotspot and NDVI differencing synergy (HANDS): A new technique for burned area mapping over boreal forest. *Remote Sensing of Environment*, 74, 362–376.
- Friedl, M. A., McIver, D. K., Hodges, J. C. F., Zhang, X. Y., Muchoney, D., Strahler, A. H., et al. (2002). Global land cover mapping from MODIS: Algorithms and early results. *Remote Sensing of Environment*, 83, 287–302.
- George, C., Rowland, C., Gerard, F., & Balzter, H. (2006). Retrospective mapping of burnt areas in Central Siberia using a modification of the normalized difference water index. *Remote Sensing of Environment*, 104, 346–359.
- Giglio, L. (2007). Characterization of the tropical diurnal fire cycle using VIRS and MODIS observations. *Remote Sensing of Environment*, 108, 407–421.
- Giglio, L., Kendall, J. D., & Tucker, C. J. (2000). Remote sensing of fires with the TRMM VIRS. *International Journal of Remote Sensing*, 21(1), 203–207.
- Giglio, L., van der Werf, G. R., Randerson, J. T., Collatz, G. J., & Kasibhatla, P. S. (2006). Global estimation of burned area using MODIS active fire observations. *Atmospheric Chemistry and Physics*, 6, 957–974.
- Hansen, M. C., DeFries, R. S., Townshend, J. R. G., Carroll, M., Dimiceli, C., & Sohlberg, R. A. (2003). Global percent tree cover at a spatial resolution of 500 meters: First results of the MODIS vegetation continuous fields algorithm. *Earth Interactions*, 7(10).
- Hansen, M. C., DeFries, R. S., Townshend, J. R. G., & Sohlberg, R. (2000). Global land cover classification at 1 km spatial resolution using a classification tree approach. *International Journal of Remote Sensing*, 21, 1331–1364.
- Ivanova, G. A., & Ivanov, V. A. (1999, June). Fire and fire regimes in the forests of central Siberia. In L. F. Neuenschwander, K. C. Ryan & G. E. Gollberg (Eds.), *Proceedings of the Joint Fire Science Conference and Workshop, Vol. 2*. (pp. 236–242). Boise, Idaho: University of Idaho and the International Association of Wildland Fire.
- Justice, C. O., Giglio, L., Korontzi, S., Owens, J., Morisette, J. T., Roy, D., et al. (2002). The MODIS fire products. *Remote Sensing of Environment*, 83, 244–262.

- Kasischke, E. S., & French, N. H. F. (1995). Locating and estimating the areal extent of wildfires in Alaskan boreal forests using multiple-season AVHRR NDVI composite data. *Remote Sensing of Environment*, 51, 263–275.
- Kasischke, E. S., Hewson, J. H., Stocks, B., van der Werf, G. R., & Randerson, J. (2003). The use of ATSR active fire counts for estimating relative patterns of biomass burning—A study from the boreal forest region. *Geophysical Research Letters*, 30(18), 1969.
- Key, C. H., & Benson, N. C. (2006). Landscape assessment (LA): Sampling and analysis methods. In D. C. Lutes, R. E. Keane, J. F. Caratti, C. H. Key, N. C. Benson, S. Sutherland & L. J. Gangi (Eds.), *FIREMON: Fire effects monitoring and inventory system. General Technical Report RMRS-GTR-164-CD* (pp. LA1–LA51). Rocky Mountain Research Station, Fort Collins, CO: United States Department of Agriculture, Forest Service [http://www.fs.fed.us/rm/pubs/rmrs\\_gtr164.pdf](http://www.fs.fed.us/rm/pubs/rmrs_gtr164.pdf), last visited: 2008, 9 September.
- Loboda, T., O’Neal, K. J., & Csizsar, I. (2007). Regionally adaptable dNBR-based algorithm for burned area mapping from MODIS data. *Remote Sensing of Environment*, 109, 429–442.
- Lopez Garcia, M. J., & Caselles, V. (1991). Mapping burns and natural reforestation using Thematic Mapper data. *Geocarto International*, 1, 31–37.
- Matson, M., & Dozier, J. (1981). Identification of subresolution high temperature sources using a thermal IR sensor. *Photogrammetric Engineering and Remote Sensing*, 47, 1311–1318.
- McCarty, J., Justice, C. O., & Korontzi, S. (2007). Agricultural burning in the southeastern United States detected by MODIS. *Remote Sensing of Environment*, 108, 151–162.
- McNab, W. H., Cleland, D. T., Freeouf, J. A., Keys, J. E., Jr., Nowacki, G. J., & Carpenter, C. A. (2007). Description of ecological subregions: Sections of the conterminous United States. Tech. Rep. WO-76B [CD-ROM] Washington, DC: United States Department of Agriculture, Forest Service.
- Miller, J. D., & Yool, S. R. (2002). Mapping forest post-fire canopy consumption in several overstory types using multi-temporal Landsat TM and ETM data. *Remote Sensing of Environment*, 82, 481–496.
- Pereira, J. M. C., Mota, B., Privette, J. L., Taylor, K. K., Silva, J. M. N., Sá, A. C. L., et al. (2004). A simulation analysis of the detectability of understory burns in miombo woodlands. *Remote Sensing of Environment*, 93, 296–310.
- Pereira, J. M. C., Vasconcelos, M. J. P., & Sousa, A. M. (2000). A rule-based system for burned area mapping in temperate and tropical regions using NOAA/AVHRR imagery. In J. L. Innes, M. Beniston, & M. M. Verstraete (Eds.), *Biomass burning and its inter-relationships with the climate system* (pp. 215–232). Dordrecht: Kluwer Academic Publishers.
- Prins, E. M., & Menzel, W. P. (1992). Geostationary satellite detection of biomass burning in South America. *International Journal of Remote Sensing*, 13, 2783–2799.
- Pu, R., Gong, P., Li, Z., & Scarborough, J. (2004). A dynamic algorithm for wildfire mapping with NOAA/AVHRR data. *International Journal of Wildland Fire*, 13, 275–285.
- Roberts, G., Wooster, M. J., Perry, G. L. W., & Drake, N. (2005). Retrieval of biomass combustion rates and totals from fire radiative power observations: Application to southern Africa using geostationary SEVIRI imagery. *Journal of Geophysical Research*, 110, D21111.
- Roy, D. P., Frost, P., Justice, C. O., Landmann, T., Roux, J. L., Gumbo, K., et al. (2005). The Southern Africa Fire Network (SAFNet) regional burned area product validation protocol. *International Journal of Remote Sensing*, 26, 4265–4292.
- Roy, D. P., Giglio, L., Kendall, J. D., & Justice, C. O. (1999). Multi-temporal active-fire based burn scar detection algorithm. *International Journal of Remote Sensing*, 20, 1031–1038.
- Roy, D. P., Jin, Y., Lewis, P. E., & Justice, C. O. (2005). Prototyping a global algorithm for systematic fire-affected area mapping using MODIS time series data. *Remote Sensing of Environment*, 97, 137–162.
- Roy, D. P., & Landmann, T. (2005). Characterizing the surface heterogeneity of fire effects using multi-temporal reflective wavelength data. *International Journal of Remote Sensing*, 26, 4197–4218.
- Roy, D. P., Lewis, P. E., & Justice, C. O. (2002). Burned area mapping using multi-temporal moderate spatial resolution data—A bi-directional reflectance model-based expectation approach. *Remote Sensing of Environment*, 83, 263–286.
- Scholes, R. J., Kendall, J. D., & Justice, C. O. (1996). The quantity of biomass burned in southern Africa. *Journal of Geophysical Research*, 101(D19), 23667–23676.
- Simon, M., Plummer, S., Fierens, F., Hoelzemann, J. J., & Arino, O. (2004). Burnt area detection at global scale using ATSR-2: The GLOBSCAR products and their qualification. *Journal of Geophysical Research*, 109, D14S02.
- Smith, A. M. S., & Wooster, M. J. (2005). Remote classification of head and backfire types from MODIS fire radiative power observations. *International Journal of Wildland Fire*, 14, 249–254.
- Stroppiana, D., Grégoire, J. -M., & Pereira, J. M. C. (2003). The use of SPOT VEGETATION data in a classification tree approach for burnt area mapping in Australian savanna. *International Journal of Remote Sensing*, 24, 2131–2151.
- Tansey, K., Grégoire, J. -M., Defourny, P., Leigh, R., Pekel, J. -F., van Bogaert, E., et al. (2008). A new, global, multi-annual (2000–2007) burnt area product at 1 km resolution. *Geophysical Research Letters*, 35, L011401.
- Tansey, K., Grégoire, J. -M., Stroppiana, D., Sousa, A., Silva, J., Pereira, J. M. C., et al. (2004). Vegetation burning in the year 2000: Global burned area estimates from SPOT VEGETATION data. *Journal of Geophysical Research*, 109(D14S03).
- Trigg, S., & Flasse, S. (2000). Characterizing the spectral-temporal response of burned savannah using *in situ* spectroradiometry and infrared thermometry. *International Journal of Remote Sensing*, 21, 3161–3168.
- Upton, G., & Cook, I. (2002). *A dictionary of statistics*. Oxford: Oxford University Press.
- Vermote, E. F., & Justice, N. Z. E. S. C. O. (2002). Operational atmospheric correction of the MODIS data in the visible to middle infrared: First results. *Remote Sensing of Environment*, 83, 97–111.
- Wolfe, R. E., Roy, D. P., & Vermote, E. (1998). MODIS land data storage, gridding, and compositing methodology: Level 2 grid. *IEEE Transactions on Geoscience and Remote Sensing*, 36, 1324–1338.